Supporting Information for

A Flexible, Microsupercapacitor with Integral Photocatalytic Fuel Cell for Self-Charging

Meijia Qiu[a, b, #], Peng Sun[a, #], Guofeng Cui[a, *], Yexiang Tong[a, *], Wenjie Mai[b, *]

[a]MOE Laboratory of Bioinorganic and Synthetic Chemistry, Key Laboratory for Polymeric Composite & Functional Materials of Ministry of Education, The Key Lab of Low-Carbon Chemistry and Energy Conservation of Guangdong Province, School of Chemistry, Sun Yat-sen University, Guangzhou, 510275, China.

[b]Siyuan Laboratory, Guangdong Provincial Engineering Technology Research Center of Vacuum Coating Technologies and New Energy Materials, Department of Physics, Jinan University, Guangzhou, 510632, China

[#] These authors contribute equally to this work

*Correspondence and requests for materials should be addressed to:

G. F. C. (email: cuigf@mail.sysu.edu.cn) or to

Y. X. T. (email: chedhx@mail.sysu.edu.cn) or to

W. J. M. (email: wenjiemai@email.jnu.edu.cn)

Calculation methods:

The areal and gravimetric capacitance C_s *and* C_g were calculated from the CV curves through the following equation:

$$C_s = \frac{\int IdU}{2vsU_w} = \frac{S}{2vsU_w}$$

$$C_g = \frac{\int IdU}{2vmU_w} = \frac{S}{2vmU_w}$$

where v is the scan rate, s and m are the surface area and mass loading of the active materials on CF, S the area of the closed CV curve and U_w is the potential window. The capacitance C can be calculated from the GCD curves through the following equations:

$$E_{GCD} = \int IUdt = IS = \frac{CU_w{}^2}{2}$$

$$C = \frac{2IS}{U_w{}^2}$$

where E_{GCD} is the energy stored during the discharging process, I is the constant current density, S is the area of the closed discharged curve from the GCD curves, C is the capacitance and U_w is the potential window.

The C_s and C_g can be gained through dividing C by the surface area and mass loading of the active materials.

The C_s of electrode and device can be gained through dividing C by the surface area of active materials and the footprint district of the MSC (as shown in Figure S12), respectively.

And the energy density and the average power density can be gained by employing the following equation:

$$E = \frac{C_{ave}U_w{}^2}{2}$$

$$P = \frac{E}{t}$$

$$t = \frac{U_w}{v}$$

in which C_{ave} is the areal or gravimetric capacitance calculated before.

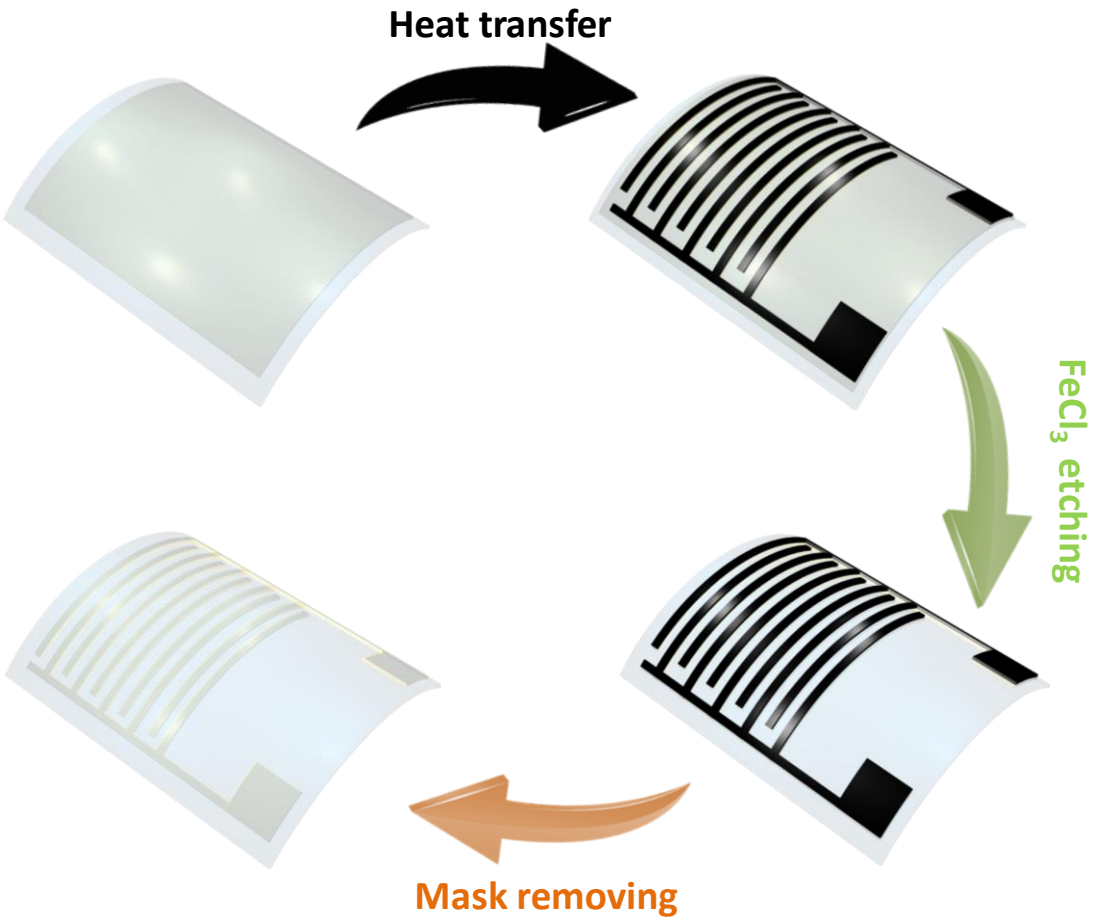

Figure S1. The fabrication process of the ITO@PET ID substrate.

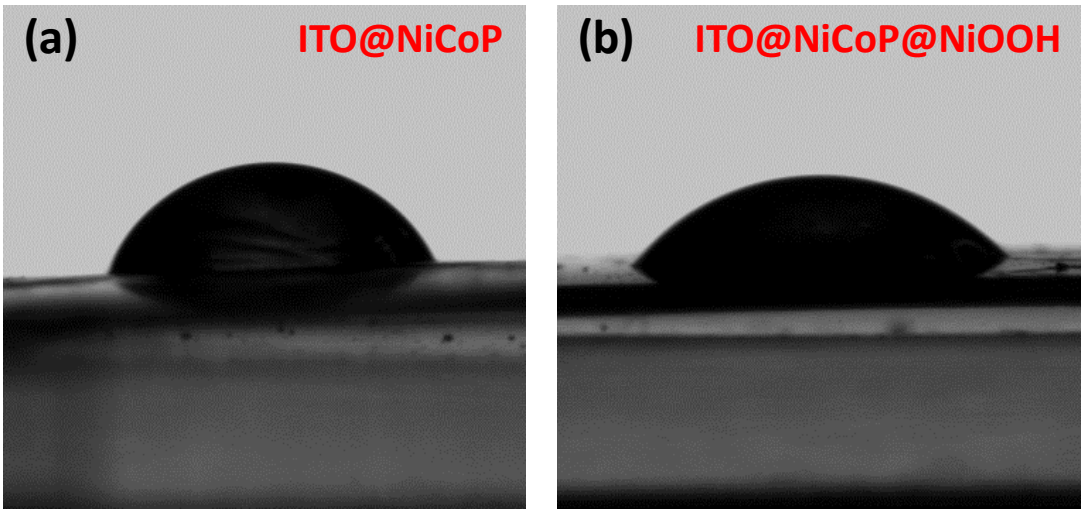

Figure S2. Water drop on the surface of (a) ITO@NiCoP and (b) ITO@NiCoP@NiOOH.

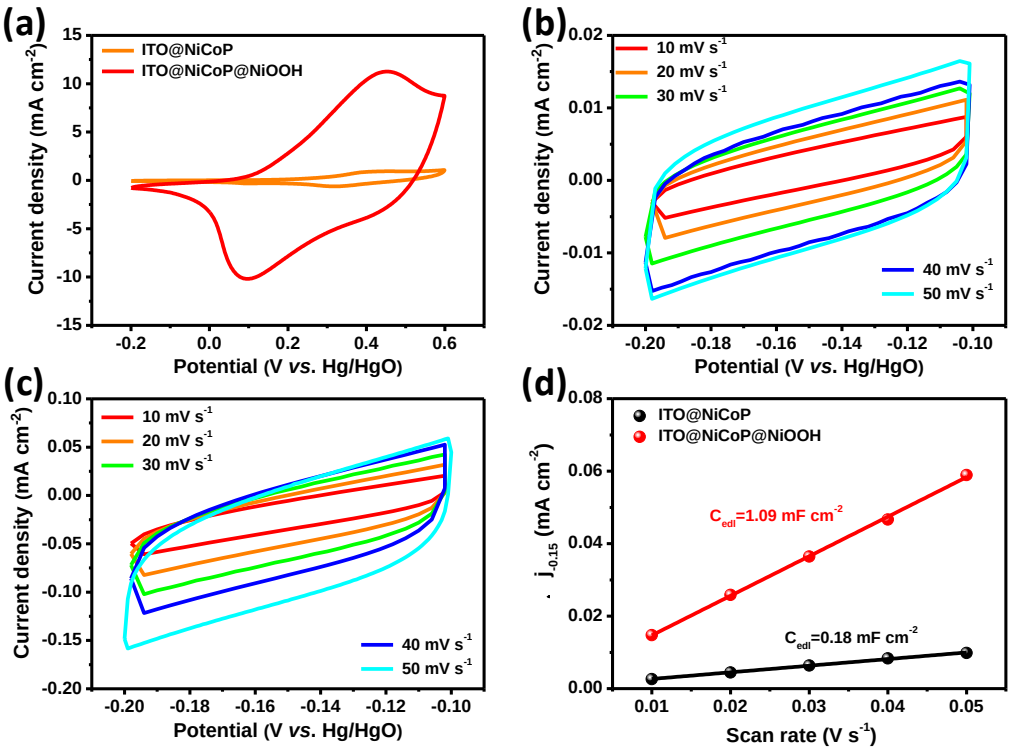

Figure S3. CV curves of the (a) ITO@NiCoP and ITO@NiCoP@NiOOH at a scan rate of 50 mV s^{-1} under a potential range of -0.2 to 0.6 V, (b) ITO@NiCoP and (c) ITO@NiCoP@NiOOH at different scan rates (10-50 mV s^{-1}) over a potential range of -0.2 to -0.1 V; (d) The capacitive current densities-scan rates calibration plots of the ITO@NiCoP and ITO@NiCoP@NiOOH.

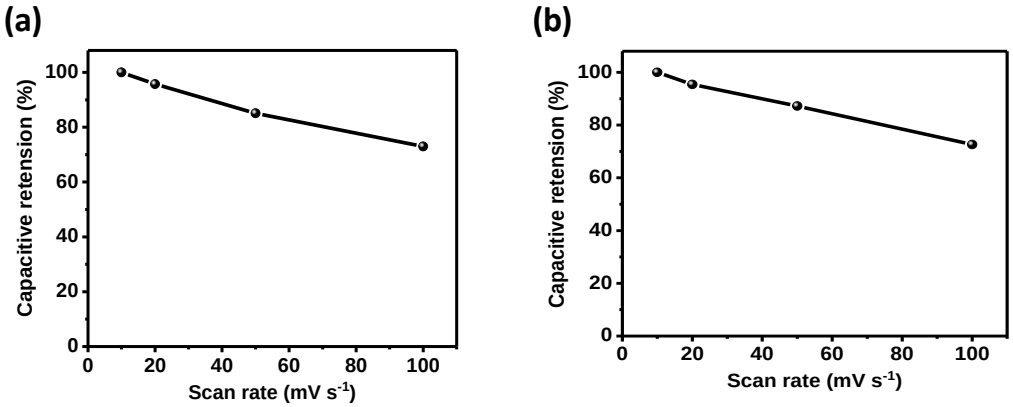

Figure S4. Rate performance of the (a) NiCoP@NiOOH positive electrode and (b) ZIF-C negative electrode under the scan rates ranging from 10 to 100 mV s^{-1}.

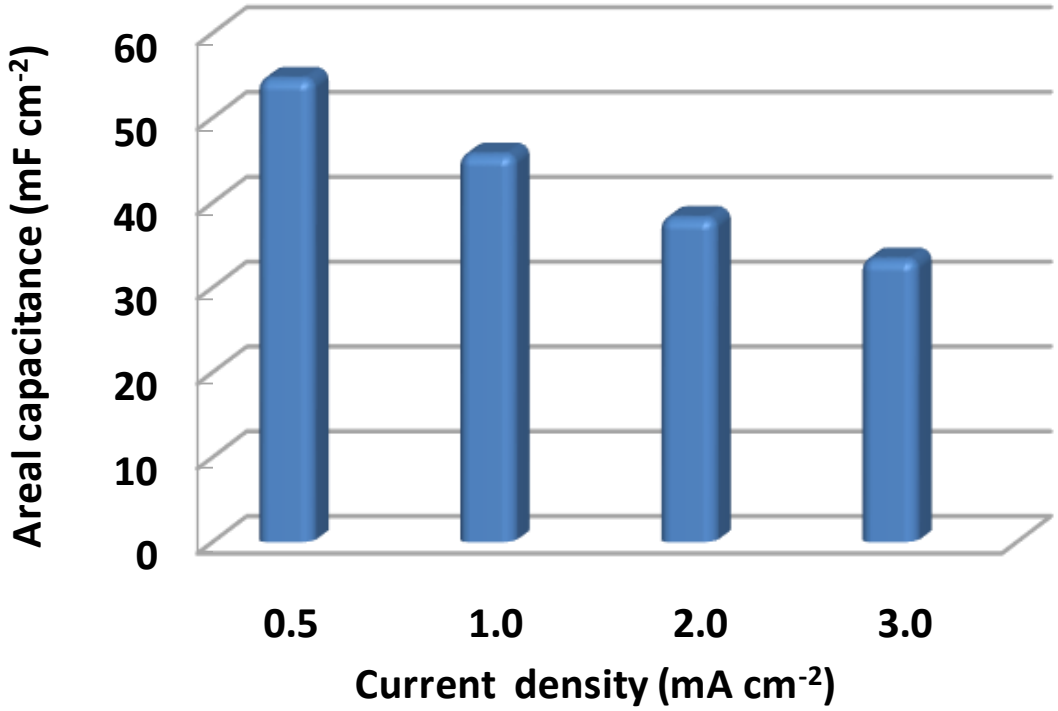

Figure S5. Rate performance of NiCoP@NiOOH//ZIF-C MSC at different current density ranging from 0.5 to 3.0 mA cm^{-2}.

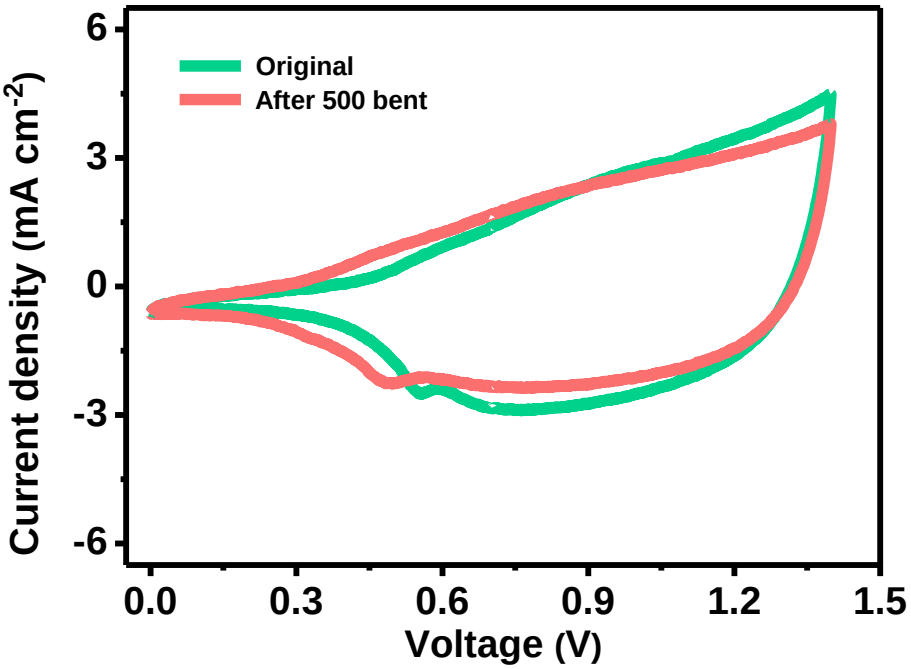

Figure S6. CV curves of the NiCoP@NiOOH//ZIF-C MSC before and after 500 bending cycles.

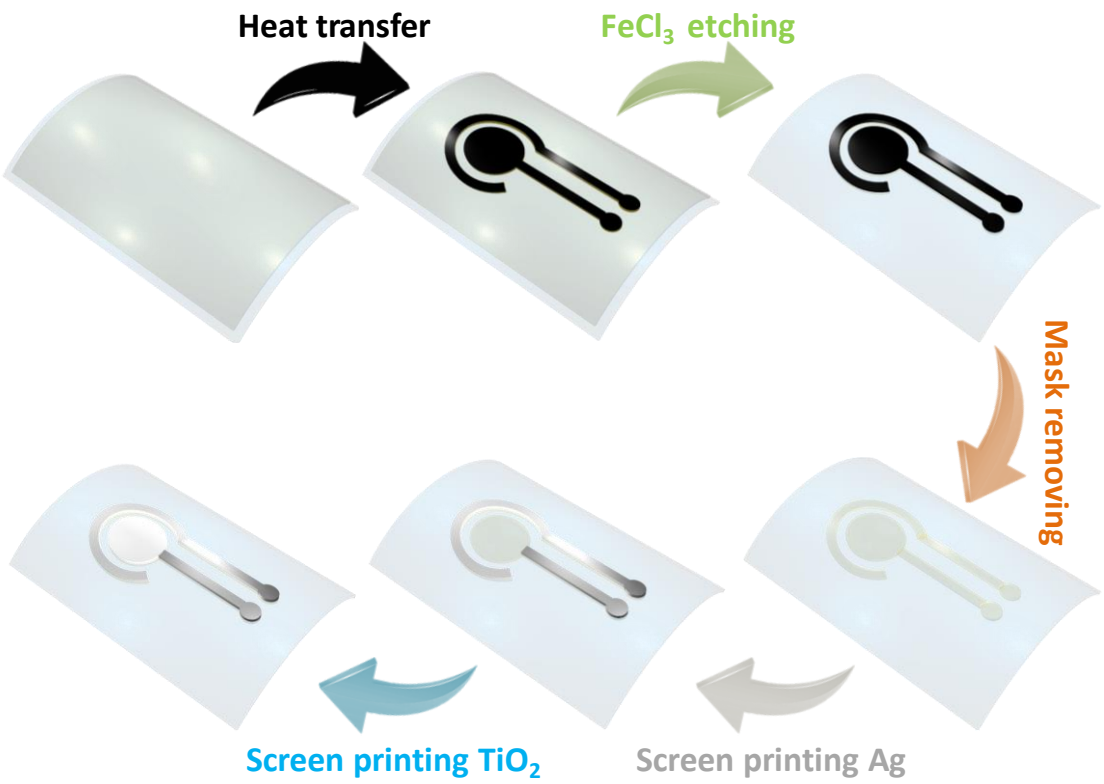

Figure S7. The fabrication process of the planer PFC.

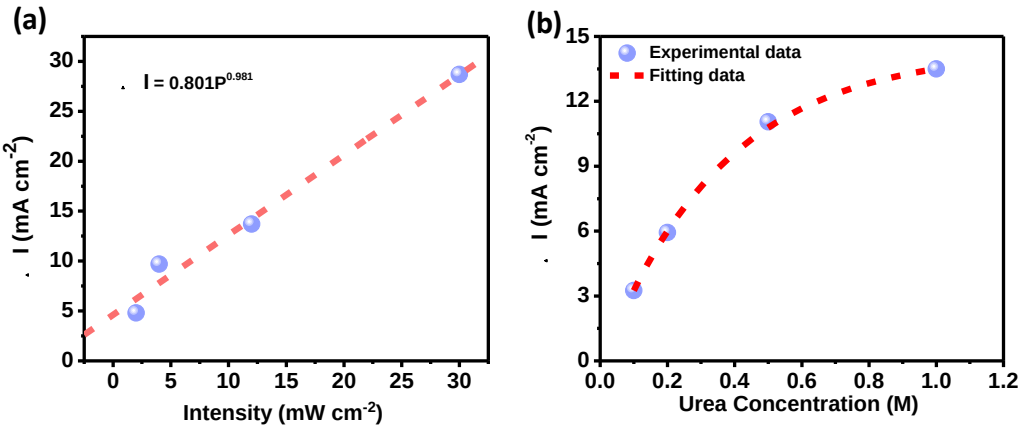

Figure S8. The net photocurrent ΔI varied with that of (a) light intensity which ranges from 2 to 30 mW cm^{-2} in 1 M urea solution and (b) urea concentration which ranges from 0.1 to 1 M under a light intensity of 12 mW cm^{-2}.

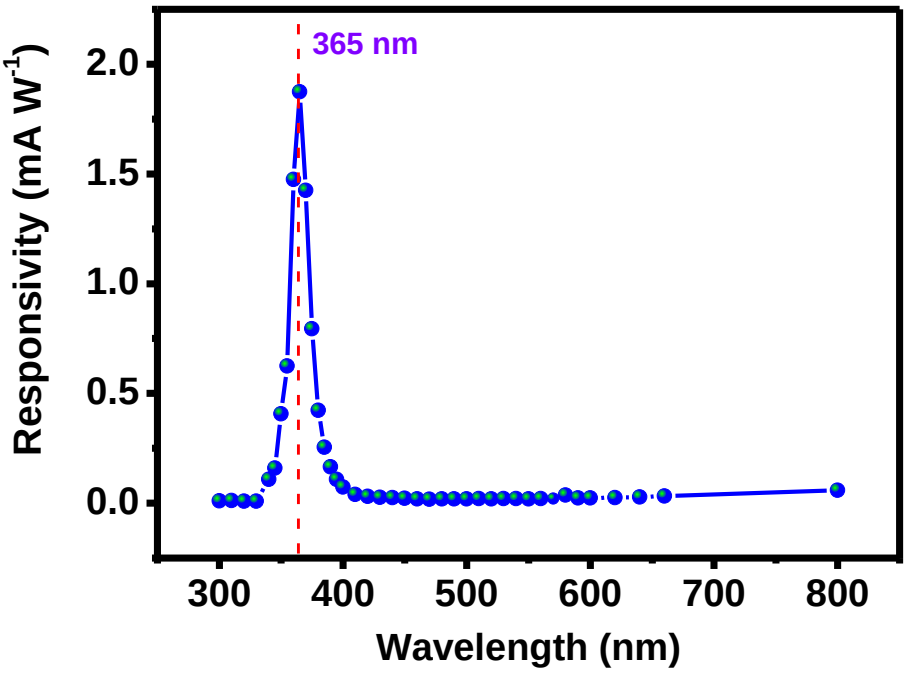

Figure S9. Typical photoresponsivity spectrum of the TiO_2 based PFC.

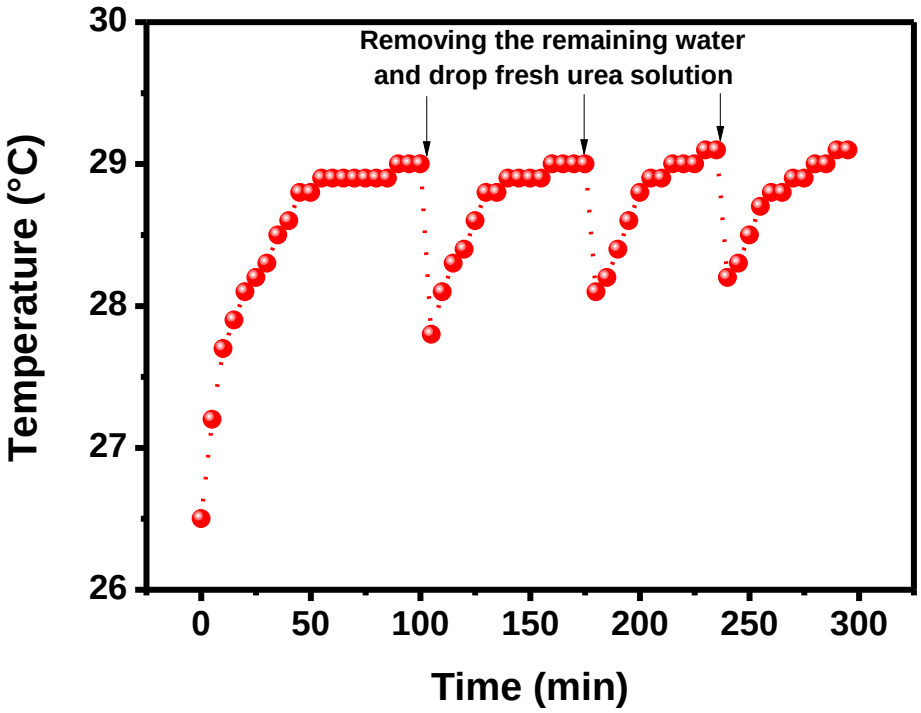

Figure S10. The temperature record of the 4 times of cyclic experiment for dropping urea after the previous drop of urea has been exhausted.

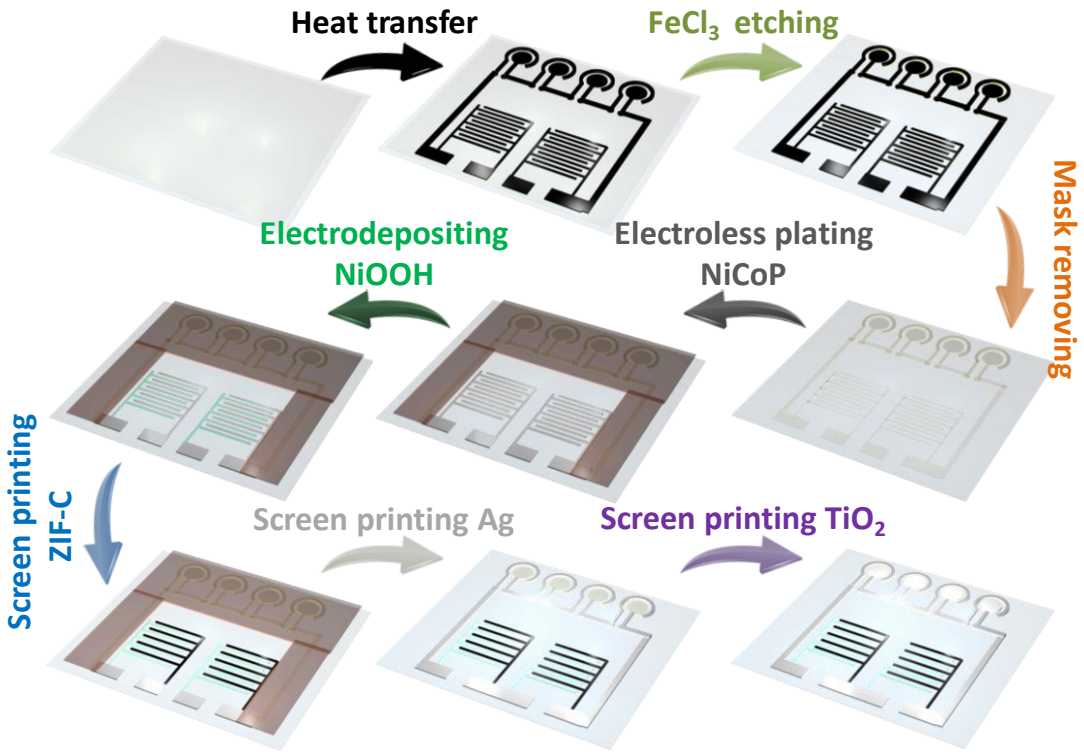

Figure S11. Scheme of the fabricated process for the all-in-one energy chip composed of four PFCs in series and two tandem MSCs.

Firstly, the as designed patterns (composed of printing ink) were printed on thermal transfer paper and then transferred to the ITO/PET substrate. Thus, the ITO/PET substrate covered by the printing ink with the designed interdigital patterns can be protected from being etched. After that, $FeCl_3$ was utilized to etch the ITO layer without protection and the printing ink was then removed, obtaining the patterned ITO layer for both MSCs and PFCs. The patterns belonging to PFCs and connecting circles were covered by Capton tape and the whole substrate was transferred into the electroless plating solution for growing NiCoP layer on ITO patterns from MSCs. The NiOOH was subsequently electrodeposited on ITO@NiCoP as positive electrode and ZIF-C was screen printed on another half of the ITO@NiCoP as negative electrode. So far, the MSCs were successfully fabricated. The Capton tape was then removed, following with the screen printing of the Ag slurry and TiO_2 slurry to finish the whole all-in-one energy chip.

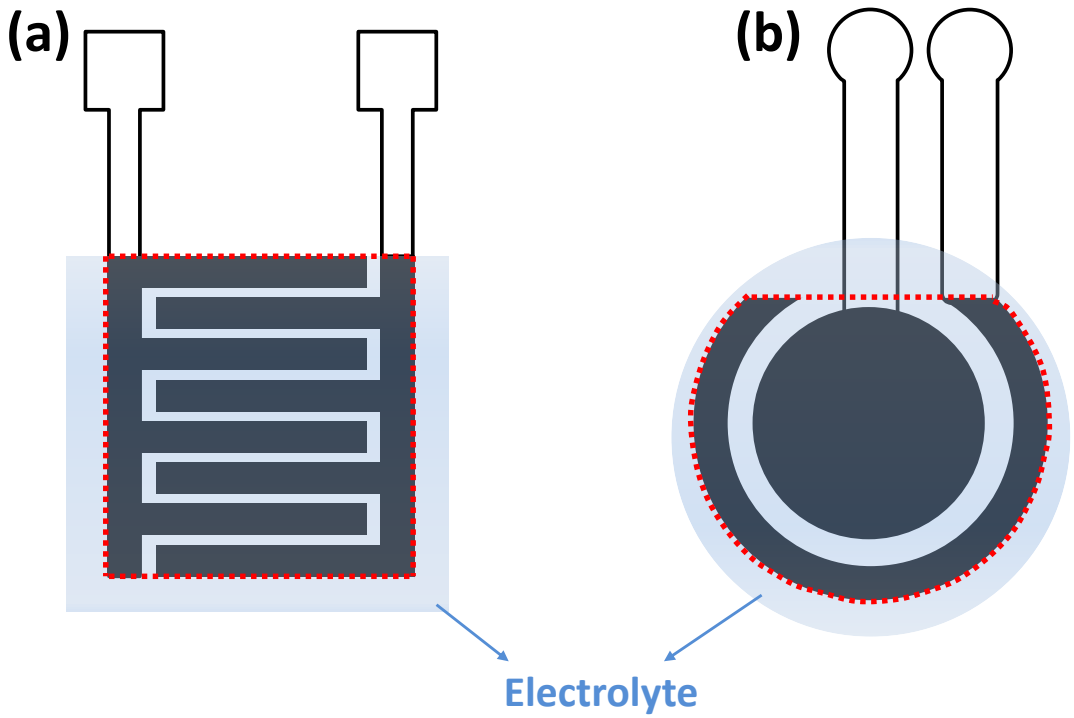

Figure S12. Scheme of the as fabricated (a) MSC and (b) PFC saturated into electrolyte, where the black part represents the area loaded with active materials.

We followed the most used method, that is, utilizing the footprint area (as shown in the whole area enclosed by red dotted box in Figure S12a) to calculate the areal capacitance. For PFCs, we followed the above method to calculate the areal power density under the situation of whole area enclosed by red dotted box in Figure S12b.

Some comparison and explanation of this work and our previous work

In this work, the performance of the NiCoP active layer is poorer than our previous work (Nano Energy 55 (2019) 506, Ni@NiCoP stretchable textile) due to the following three reasons: Firstly, the previous work deposited a Ni conductive layer between the spandex and NiCoP layer. The square resistance of the Ni layer was measured to be nearly 6.0 Ω sq^{-1}, which is lower than that of ITO layer (15 Ω sq^{-1}) in this work. This is helpful for enhancing the electrochemical performance of the NiCoP active layer. Secondly, the wettability of the ITO@NiCoP and Ni@NiCoP stretchable textile exists large difference, as presented in Figure S13. For ITO@NiCoP, the contact angle was calculated to be 66.22° (Figure S13a). However, the water drop can be instantly absorbed by the Ni@NiCoP stretchable textile, as shown in Figure S13b and S13c. Thus, the Ni@NiCoP stretchable textile owns much better wettability in solution than the ITO@NiCoP, which is beneficial for better contact between the electrode and electrolyte. Finally, the electrochemical double layer capacitances C_{edl} (proportional to the ECSA) of the two kinds of electrodes were also analyzed through CV method. Non-faradaic region can be chosen as -0.2 V to -0.1 V according to Figure S14a. Under this potential range, CV curves with different scan rates were measured, as presented in Figure S14b and S14c. Through linear fitting of the capacitive charge/discharge current and scan rate (Figure S14d), the C_{edl} of the ITO@NiCoP and the Ni@NiCoP stretchable textile can be calculated to be 0.18 mF cm^{-2} and 6.47 mF cm^{-2}, respectively. This result indicates that the Ni@NiCoP stretchable textile possesses much more active sites for electrochemical energy storage than the ITO@NiCoP, thus reaching higher capacitance.

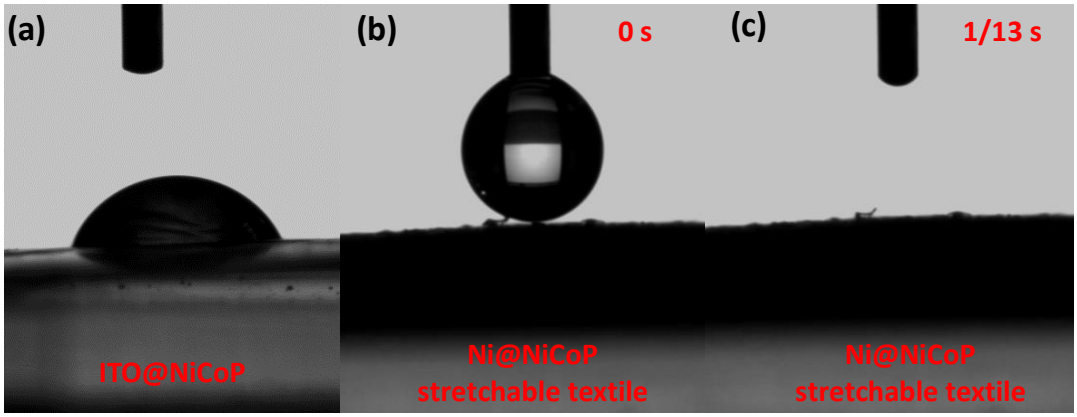

Figure S13. Water drop on the surface of (a) ITO@NiCoP and Ni@NiCoP stretchable textile (camera recorded) at (b) 0 s and (c) 1/13 s.

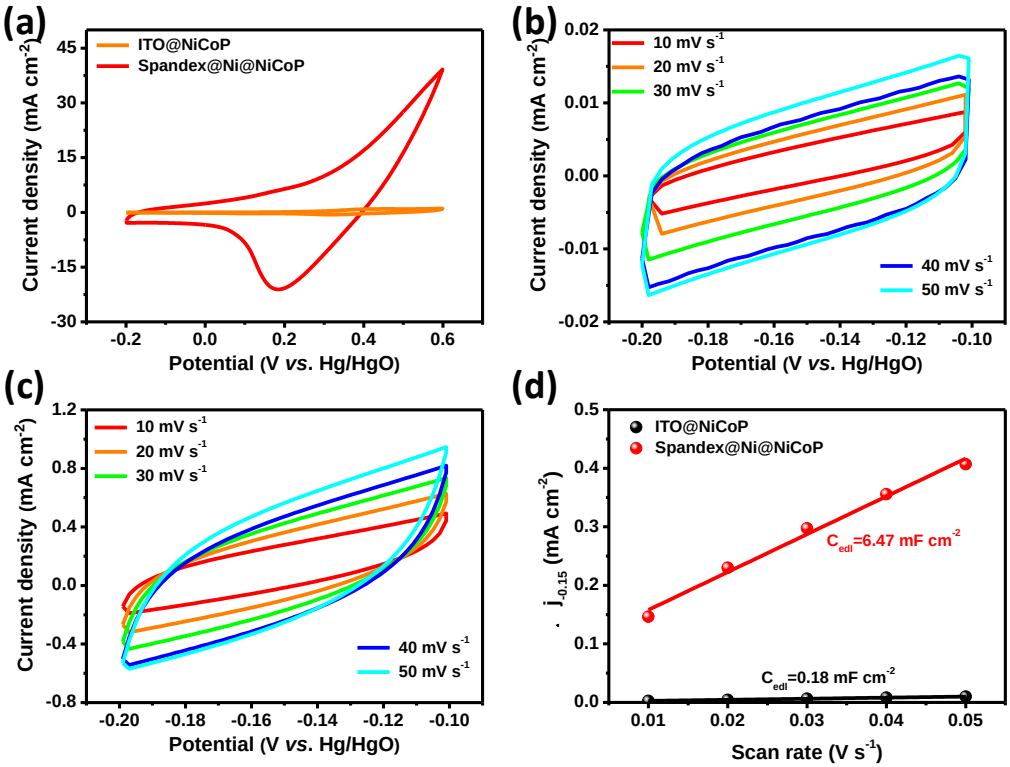

Figure S14. CV curves of the (a) ITO@NiCoP and Ni@NiCoP stretchable textile at a scan rate of 50 mV s^{-1} under a potential range of -0.2 to 0.6 V, (b) ITO@NiCoP and (c) Ni@NiCoP stretchable textile at different scan rates (10-50 mV s^{-1}) over a potential range of -0.2 to -0.1 V; (d) The capacitive current densities-scan rates calibration plots of the ITO@NiCoP and Ni@NiCoP stretchable textile.

Table S1. Capacitance comparison between previous work and this work.

Name	Test Condition	Capacitance	Reference
cellular graphene MSCs	5 mV s^{-1}	2.5 mF cm^{-2}	1
Ni-MnO_2 paper MSCs	30 mV s^{-1}	2.2 mF cm^{-2}	2
MnO_2-PPy MSCs	10 mV^{-1}	7.3 mF cm^{-2}	3
V_2O_5-PANI MSCs	10 mV^{-1}	6.4 mF cm^{-2}	3
MoS_2@rGO-CNT MSCs	0.1 mA cm^{-2}	13.7 mF cm^{-2}	4
coral Ni@MnO_2 MSCs	5 mV s^{-1}	52.7 mF cm^{-2}	5
$Cu(OH)_2$@FeOOH MSCs	1 mA cm^{-2}	58.0 mF cm^{-2}	6
Cu-HCF/graphene//Fe-HCF/graphene AMSCs	0.75 mA cm^{-2}	19.8 mF cm^{-2}	7
LSG/Ni-CAT MOF MSC	0.2 mA cm^{-2}	15.2 mF cm^{-2}	8
VN//MnO_2 AMSCs	1 mV s^{-1}	16.1 mF cm^{-2}	9
Ppy@multi-walled CNT AMSCs	0.1 mA cm^{-2}	21.8 mF cm^{-2}	10
NiCoP@NiOOH//ZIF-C AMSC	10 mV^{-1}; 0.5 mA cm^{-2}	43.2 mF cm^{-2}; 54.7 mF cm^{-2}	This work

Table S2. The mass loading of the NiCoP (one side), NiOOH and ZIF-C.

Materials / Number	NiCoP (mg) (one side)	NiOOH (mg)	ZIF-C (mg)
1	1.03	0.15	0.59
2	1.06	0.13	0.55
3	0.98	0.08	0.54
4	1.04	0.15	0.58
5	1.09	0.16	0.55
Average	1.04	0.13	0.56

Reference

(1) Shao, Y. L.; Li, J. M.; Li, Y. G.; Wang, H. Z.; Zhang, Q. H.; Kaner, R. B. Flexible Quasi-Solid-State Planar Micro-Supercapacitor Based on Cellular Graphene Films. *Mater. Horiz.* **2017,** *4*, 1145-1150.

(2) Guo, R. S.; Chen, J. T.; Yang, B. J.; Liu, L. Y.; Su, L. J.; Shen, B. S.; Yan, X. B. In-Plane Micro-Supercapacitors for an Integrated Device on One Piece of Paper. *Adv. Funct. Mater.* **2017,** *27*, 1702394.

(3) Yue, Y.; Yang, Z.; Liu, N.; Liu, W.; Zhang, H.; Ma, Y.; Yang, C.; Su, J.; Li, L.; Long, F.; Zou, Z.; Gao, Y. A Flexible Integrated System Containing a Microsupercapacitor, a Photodetector, and a Wireless Charging Coil. *ACS Nano* **2016,** *10*, 11249-11257.

(4) Yang, W.; He, L.; Tian, X.; Yan, M.; Yuan, H.; Liao, X.; Meng, J.; Hao, Z.; Mai, L. Carbon-MEMS-Based Alternating Stacked MoS_2 @rGO-CNT Micro-Supercapacitor with High Capacitance and Energy Density. *Small* **2017,** *13*, 1700639.

(5) Lin, Y.; Gao, Y.; Fan, Z. Printable Fabrication of Nanocoral-Structured Electrodes for High-Performance Flexible and Planar Supercapacitor with Artistic Design. *Adv. Mater.* **2017,** *29*, 1701736.

(6) Xie, J.; Ji, Y.; Kang, J.; Sheng, J.; Mao, D.; Fu, X.; Sun, R.; Wong, C. *In Situ* Growth of $Cu(OH)_2$@FeOOH Nanotube Arrays on Catalytically Deposited Cu Current Collector Patterns for High-Performance Flexible In-Plane Micro-Sized Energy Storage Devices. *Energy Environ. Sci.* **2019,** *12*, 194-205.

(7) He, Y.; Zhang, P.; Wang, M.; Wang, F.; Tan, D.; Li, Y.; Zhuang, X.; Zhang, F.; Feng, X. Nano-Sandwiched Metal Hexacyanoferrate/Graphene Hybrid Thin Films for In-Plane Asymmetric Micro-Supercapacitors with Ultrahigh Energy Density. *Mater. Horiz.* **2019,** *6*, 1041-1049.

(8) Wu, H.; Zhang, W.; Kandambeth, S.; Shekhah, O.; Eddaoudi, M.; Alshareef, H. N. Conductive Metal–Organic Frameworks Selectively Grown on Laser‐Scribed Graphene for Electrochemical Microsupercapacitors. *Adv. Energy Mater.* **2019,** *9*, 1900482.

(9) Qin, J. Q.; Wang, S.; Zhou, F.; Das, P.; Zheng, S. H.; Sun, C. L.; Bao, X. H.; Wu, Z. S. 2D Mesoporous MnO_2 Nanosheets for High-Energy Asymmetric Micro-Supercapacitors in Water-In-Salt Gel Electrolyte. *Energy Storage Materials* **2019,** *18*, 397-404.

(10) Gao, J.; Shao, C.; Shao, S.; Wan, F.; Gao, C.; Zhao, Y.; Jiang, L.; Qu, L. Laser-Assisted Large-Scale Fabrication of All-Solid-State Asymmetrical Micro-Supercapacitor Array. *Small* **2018,** *14*, 1801809.